POLITECNICO DI TORINO
Repository ISTITUZIONALE

Guaranteed Torque and Demagnetization Current During Active Short-Circuit Transients of PMSMs

Original
Guaranteed Torque and Demagnetization Current During Active Short-Circuit Transients of PMSMs / Olson, G.F., Ferrari, S., Bojoi, A., Pescetto, P., Peretti, L., Pellegrino, G.. - (2024), pp. 1-8. (2024 IEEE International Conference on Industrial Technology (ICIT) Bristol (UK) 25-27 March 2024) [10.1109/icit58233.2024.10540677].

Availability:
This version is available at: 11583/2989362 since: 2024-06-06T19:58:57Z

Publisher:
IEEE

Published
DOI:10.1109/icit58233.2024.10540677

Terms of use:

This article is made available under terms and conditions as specified in the corresponding bibliographic description in the repository

Publisher copyright
IEEE postprint/Author's Accepted Manuscript

©2024 IEEE. Personal use of this material is permitted. Permission from IEEE must be obtained for all other uses, in any current or future media, including reprinting/republishing this material for advertising or promotional purposes, creating new collecting works, for resale or lists, or reuse of any copyrighted component of this work in other works.

(Article begins on next page)

25 November 2026

Guaranteed Torque and Demagnetization Current During Active Short-Circuit Transients of PMSMs

1st Gustaf Falk Olson
Electric Power and Energy Systems
Royal Institute of Technology, KTH
Stockholm, Sweden
gufo@kth.se

2nd Simone Ferrari
Department of Energy G. Ferraris
Politecnico di Torino
Turin, Italy
simone.ferrari@polito.it

3rd Andrei Bojoi
Department of Energy G. Ferraris
Politecnico di Torino
Turin, Italy
andrei.bojoi@polito.it

4th Paolo Pescetto
Department of Energy G. Ferraris
Politecnico di Torino
Turin, Italy
paolo.pescetto@polito.it

5th Luca Peretti
Electric Power and Energy Systems
Royal Institute of Technology, KTH
Stockholm, Sweden
lucap@kth.se

6th Gianmario Pellegrino
Department of Energy G. Ferraris
Politecnico di Torino
Turin, Italy
gianmario.pellegrino@polito.it

***Abstract*—Active short-circuit is a standard emergency procedure applied to three-phase permanent-magnet synchronous machine drives in battery-electric and hybrid electric drivetrains to comply with stringent automotive safety standards, such as the ISO 26262. Unfortunately, the ensuing torque and current transients can harm the passengers and the driveline itself. This paper develops and validates a mathematical and graphical method to determine the safe operating area of pre-fault current conditions to guarantee that the torque remains within user-defined acceptable bounds and that the permanent magnets do not demagnetize during the short-circuit transient. The new method utilizes an inductance-based dynamic model of the motor, including magnetic saturation. The proposed methodology promises to be useful in the design, initial testing, and commissioning of permanent-magnet synchronous machines used for the propulsion of automobiles.**

***Index Terms*—active short-circuit, cross saturation, demagnetization, PMSM, uncontrolled generation.**

I. Introduction

Fail safe operation in electric vehicles (EVs) is a critical aspect to consider when developing the electric drivetrain in order to comply with functional safety standards such as the ISO26262 [1]. An active short-circuit (ASC) is applied in a permanent-magnet synchronous machine (PMSM) inverter in response to an imminent or already occurred fault to protect the application from a catastrophic failure [2]–[5]. In EVs, for example, a high-level control unit may take this decision due to battery overheating or a brake failure. An ASC is the alternative to inverter shutdown, which is the least harmful inverter-fault condition. However, it cannot be applied for all speeds due to the risk of harmful uncontrolled generation (UCG) voltage [6]. The ASC has also been proposed as a mitigating action to other drive-initiated faults such as single-phase short-circuits [4]. It is considered a safe state of the motor and inverter since no current flows at standstill and, hence, there will be no torque. At a fixed and sufficiently high speed, on the other hand, the steady-state short-circuit current (SSC) equals the characteristic current, but the torque remains low because the SSC is acting predominantly in the demagnetizing direction. Notwithstanding the SSC, the transient between regular operation and SSC is critical, because of the potentially large demagnetization currents and torque pulsations. Transient short-circuit currents can lead to irreversible demagnetization of PMSMs and, even more, of permanent magnet (PM)-assisted synchronous reluctance machines (SyRs) machines [7]. It can also venture the inverter. Torque pulsations, on the other hand, may put the driver at risk and/or cause stresses on mechanical structures unless appropriate actions are taken [4]. As the ASC constitutes a deliberately imposed condition with high economic and safety risks, it requires careful testing and, possibly, imposes constraints on the machine design to ensure that the potential damages are limited [4]. However, constraining the design space is undesirable and should be avoided, if possible.

To date, methods to evaluate the transient short-circuit currents have been developed [3], [4]. Analytical models at linear magnetic conditions are declared in [3] and finite element (FE) simulations accounting for saturation corroborate the findings. This paper provides useful insights into the transient behavior of d-current and torque and their dependency on electrical parameters, initial conditions, and saturation. At linear magnetic conditions, the d- and q-axis inductances, L_d and L_q, are constant. For this condition, it is found that the peak transient d-current decays with the armature time constant, $\tau_a = {2L_dL_q}/{(R_s(L_d+L_q))}$, with R_s being the stator resistance. Oppositely, the peak transient current increases with the PM magnetization [5], and the nominal saliency ratio, $\xi = {L_q}/{L_d}$, for a fixed characteristic current and PM flux linkage [3]. Generally, it also increases with the loading, which can be seen as a result of the increased flux linkage magnitude along the maximum-torque-per-ampere (MTPA) trajectory [5].

Reference [3] further demonstrates that magnetic saturation significantly impacts the peak demagnetization current and

torque, which emphasizes the importance of modeling the machine's (cross-) saturation. To this end, a flux-map-based evaluation is carried out in [5]. As opposed to [3], it introduces a general method to compute the current, flux linkage, and electromagnetic torque trajectories at non-linear magnetic conditions during the ASC transient. When presented graphically, the results give interpretable evidence as to how the salience, PM magnetization, and initial loading affect the peak transient current. A straightforward method to calculate the hyper worst-case short-circuit current is proposed. However, this value is overly conservative as it assumes a lossless, undampened decay of the flux linkages at constant speed.

The aforementioned papers all provide methods to assess the risk of demagnetization and to estimate the torque pulsations. To clamp the peak phase-current during an ASC a two-stage process is proposed in [2]. It is a step taken in the direction of minimizing the peak demagnetization current during the transient without using a machine model, but the method assumes that the process is initiated when the PMSM is at no-load, which is an optimistic scenario.

Altogether, we conclude that a reliable method to determine a safe set of initial operating points (i.e. the initial condition of the ASC) currently is missing. This is one of the main obstacles to defining a strategy for mitigating the possibly detrimental effects of ASC transients. The primary goals of such a strategy should be to guarantee that the peak current does not exceed the demagnetization current and to constrain the torque pulsations during the transient. For this reason, this paper presents a graphical/mathematical method to compute a set of initial conditions that ensures that the demagnetization current and a user-defined maximum torque are bounded during the transient to the SSC. We also outline how it can be used practically to avoid exceeding these limits. The method relies on offline calculations using flux maps to account for magnetic saturation, which has proven to produce accurate results of the machine states [5]. The identification of the flux maps through both finite-element analysis (FEA) [8] and experiments [9] is thoroughly described in the literature.

The remainder of this paper is organized as follows. Section II presents the flux-map-based short-circuit model. Section III introduces the proposed method for calculating the set of feasible initial conditions of the ASC transient. Section IV validates the method versus an open-source simulation software whose accuracy in reproducing the ASC transient has been verified against experiments for the PMSM under test. Section V concludes the main findings.

II. Short-Circuit Model Based On Flux Maps

This section presents the dynamic short-circuit model of a three-phase PMSM. First, the linear system is introduced before the flux-map-based non-linear dynamic model is presented. By selecting the dq-currents as state variables, their dynamics are easily obtained without the use of inverse flux maps. Moreover, the electromechanical torque equation is easily applied. These virtues facilitate the development and implementation of the ASC strategy presented in the next section. The section ends by explaining how to calculate the SSC for both models.

A. State-Space Model: Linear Magnetic Conditions

The linear state-space model in the rotor reference-frame, (2), emerges from the stator voltage equation (1).

$$\begin{aligned}\bar{u}_{dq} &= \boldsymbol{R}_s \bar{i}_{dq} + \frac{d\left(\boldsymbol{L}_s \bar{i}_{dq} + \bar{\psi}_{r,dq}\right)}{dt} \\ &\quad + \omega_r \boldsymbol{J}\left(\boldsymbol{L}_s \bar{i}_{dq} + \bar{\psi}_{r,dq}\right)\end{aligned} \tag{1}$$

$$\begin{aligned}\frac{d\bar{i}_{dq}}{dt} = \begin{bmatrix} L_d^{-1} & 0 \\ 0 & L_q^{-1} \end{bmatrix} \Bigg(\underbrace{\begin{bmatrix} -R_s & \omega_r L_q \\ -\omega_r L_d & -R_s \end{bmatrix}}_{\boldsymbol{A}} \bar{i}_{dq} \\ + \bar{u}_{dq} - \bar{e}_{dq} \Bigg)\end{aligned} \tag{2}$$

Here, $\bar{u}_{dq}$ and $\bar{i}_{dq}$ are the real-valued stator voltage and current space-vectors, $\bar{\psi}_{r,dq}$ the rotor flux linkage, and $\bar{e}_{dq}$ the back electro-motive force (emf). ω_r is the rotor electrical speed, which is calculated from the mechanical speed, ω_m, and pole-pair number, p, as $\omega_r = p\omega_m$. The bold-font letters denote matrices. Specifically, $\boldsymbol{R}_s = \text{diag}\left([R_s, R_s]\right)$ is the stator resistance matrix, $\boldsymbol{L}_s = \text{diag}\left([L_d, L_q]\right)$ is the inductance matrix, and $\boldsymbol{J}$ is a $\pi/2$ rad rotation-matrix. Unless the rotor is isotropic, as in a surface permanent-magnet machine, $L_d \neq L_q$.

The presented equations are valid independent of the adopted definition of the dq-axes orientation. Henceforth, the PM-convention is adopted in this paper, i.e. the d-axis is aligned with the flux of the rotor magnets, and the q-axis is in the direction of minimal reluctance. Hence, the rotor flux linkage is $\bar{\psi}_{r,dq}^T = [\psi_{PM},\ 0]$ by definition, where ψ_{PM} denotes the PM flux linkage. It ensues that $\bar{e}_{dq}^T = [0,\ \omega_r \psi_{PM}]$.

B. State-Space Model: Non-Linear Magnetic Conditions

To model the non-linearities of the d- and q-axes flux linkages, ψ_d and ψ_q, invoked by the magnetic steel saturation, flux maps can be identified as functions of $\bar{i}_{dq}$ [8], [9]. They constitute lookup tables, which generally can be defined as in (3), where the boldface symbols represent lookup tables with the inputs within parentheses.

$$\begin{cases} \psi_d = \boldsymbol{\Psi_d}(i_d, i_q) \\ \psi_q = \boldsymbol{\Psi_q}(i_d, i_q) \end{cases} \tag{3}$$

When the machine is subjected to saturation, the stator voltage equations in (1) need to account for the time derivatives of the current-inductance products and PM flux. The governing state-space equation, (4), results from applying the product rule for derivatives.

$$\begin{aligned}\frac{d\bar{i}_{dq}}{dt} &= \boldsymbol{L}_{SyR}^{-1}\left(\boldsymbol{A}\bar{i}_{dq} + \bar{u}_{dq} - \bar{e}_{dq}\right), \\ \boldsymbol{L}_{SyR} &= \begin{bmatrix} l_{dd}\bar{i}_d + L_d\bar{i}_d + \psi_{dd} & l_{dq}\bar{i}_d + \psi_{qq} \\ l_{qd}\bar{i}_q & l_{qq}\bar{i}_q + L_q \end{bmatrix}\end{aligned} \tag{4}$$

For compactness, the incremental inductances $l_{xy}(i_d, i_q) = {}^{\partial L_x(i_d,i_q)}/_{\partial i_y}$ and the PM-flux partial derivatives $\psi_{xx}(i_d, i_q) =$

$\partial\psi_{PM}(i_d,i_q)/\partial i_x$ have been introduced. The chord-slope inductances $L_x(i_d,i_q) \triangleq \Psi_x(i_d,i_q)/I_x$ are now functions of the d- and q-currents. Henceforth, the arguments of the parameter maps are omitted for better readability.

Deliberately, we choose $\bar{i}_{dq}$ as our state variables despite the need to calculate the incremental inductances. However, flux maps can easily be manipulated to calculate the required partial derivatives of the chord-slope inductances and PM flux-linkages numerically from finite differences. The formulation in (4) is convenient because it allows drawing the phase-portrait of the currents. It will subsequently be used when evaluating the ASC transients in the upcoming section.

Finally, the average torque from the time-fundamental current in an m_s-phase machine can be calculated by performing element-wise multiplications of the flux maps with the rectangular current grids, $\boldsymbol{I}_d$ and $\boldsymbol{I}_q$, defining the (i_d, i_q) domain over which the flux maps have been identified:

$$\boldsymbol{\tau}_e = \frac{m_s p}{2} \left(\boldsymbol{\Psi}_d \odot \boldsymbol{I}_q - \boldsymbol{\Psi}_q \odot \boldsymbol{I}_d \right). \tag{5}$$

Over a mechanical period, torque ripple will also manifest due to the change in the coenergy with the rotor position, θ_r [10]. Its instantaneous value is declared in (6). The coenergy can be expressed using either $\bar{i}_{dq}$ or $\bar{i}_{abc}$ as the independent current variable employing an appropriate coordinate transformation.

$$\Delta\tau_e(\theta_r) = \frac{\partial W_c}{\partial \theta_r}\left(\bar{I}_{dq}, \theta_r\right) - \boldsymbol{\tau}_e(\bar{I}_{dq}), \tag{6}$$
$$W_c\left(\bar{I}_{abc}, \Theta_r\right) = \sum_{j=1}^{m} \int_0^{I_j} \psi_j(i_j, \Theta_r) di_j$$

C. Steady-State Short-Circuit Current

The SSC at a fixed speed is obtained by setting the current time-derivative vector and $\bar{u}_{dq}$ to zero in (2) for a linear model and in (4) for a non-linear model. The linear model possesses the analytical solution in (7).

$$\bar{i}_{dq} = \begin{bmatrix} -L_q \psi_{PM} / \left[L_d L_q + (R_s/\omega_r)^2 \right] \\ -\omega_r R_s \psi_{PM} / \left(L_d L_q \omega_r^2 + R_s^2 \right) \end{bmatrix} \tag{7}$$

This equation gives a useful heuristic rule for distinguishing between low-speed and high-speed operation. The latter is characterized by $R_s^2 << L_d L_q \omega_r^2$. As the speed increases, the SSC converges to the characteristic current, $i_{\text{ch}} = \psi_{\text{PM}}/L_d$, aligned with the d-axis to demagnetize the machine. Thus, at high speed, the SSC is practically independent of the speed.

On the contrary, the SSC for the non-linear model must be obtained from a numerical method. The Gauss-Newton method, (8), updates the initial guess, $\bar{i}_{dq}^{(0)}$, of the SSC until some update condition is met at iteration k. E.g. the iterations are stopped once $\|\Delta\bar{i}_{dq}^{(k)}\|_2$ is below a tolerance threshold.

$$\bar{i}_{dq}^{(k+1)} = \bar{i}_{dq}^{(k)} - \underbrace{\mathbf{J}^{-1}\left(\bar{i}_{dq}^{(k)}\right) \bar{f}\left(\bar{i}_{dq}^{(k)}\right)}_{\Delta\bar{i}_{dq}^{(k)}}, \tag{8}$$
$$\bar{f}\left(\bar{i}_{dq}^{(k)}\right) = \boldsymbol{A}\bar{i}_{dq} - \bar{e}_{dq},$$
$$\mathbf{J}\left(\bar{i}_{dq}^{(k)}\right) = \begin{bmatrix} -R_s + \omega_r\left(i_q l_{qd}\right) & \omega_r\left(L_q + l_{qq} i_q\right) \\ -\omega_r(L_d + l_{dd} i_d + \psi_{dd}) & -R_s - \omega_r(i_d l_{dq} + \psi_{qq}) \end{bmatrix}$$

Note that the Jacobian, $\mathbf{J}\left(\bar{i}_{dq}\right)$, of the function $\bar{f}\left(\bar{i}_{dq}\right)$ in (8) is obtained analytically and can be supplied to the Gauss-Newton algorithm rather than estimated from finite differences. The function $\bar{f}\left(\bar{i}_{dq}\right)$ results from setting the time-derivative and $\bar{u}_{dq}$ to zero in (4). The SSC of the non-linear model is obtained as $\bar{i}_{dq}^{(K+1)}$ when the stopping condition is fulfilled after iteration $k = K$.

D. Manipulation of Experimental Inductance Maps

Experimentally identified flux maps are preferable to FEA generated counterparts from a predictive validity standpoint. However, experimental maps are typically corrupted by noise, which may lead to discontinuities and distortions of the derived apparent inductance maps and their partial derivatives. Therefore, the inductance maps that are derived from experiments in this paper have been manipulated to remove these distortions. To smoothen the $L_{dq}(\bar{i}_{dq})$-maps the maps are interpolated using a shape-preserving piecewise cubic hermite interpolating polynomial (PCHIP). It is first applied to $L_d(\bar{i}_{dq})$ and $L_q(\bar{i}_{dq})$ for each value of i_d whereby any potential outliers that do not preserve monotonicity of the inductance function are removed. Then the same type of interpolation is carried out for each value of i_q. In practice, this method gave satisfactory properties of the resulting inductance maps, especially continuous partial derivatives in all directions.

Finally, the maps may only encompass parts of the ASC transient, which typically extends beyond the normal operating region. Thus, the maps need to be extended into an enlarged operating area. A linear extrapolation is chosen for this purpose in this paper.

III. Active Short-Circuit: Safe Initial States

To comply with safety demands according to the ISO26262 standard and salvage the PMs from demagnetization, two constraints on the ASC transient can be acknowledged, namely: (1) not to exceed the demagnetization current, $|i_{d,\text{demag}}|$, and (2) not to exceed a user-defined maximum torque $|\tau_{e,\max}|$ at any time during the transient. To that end, we begin by describing the machine under test (MUT) in Section III-A. Section III-B reports the speed criterion which warrants an ASC in place of an inverter shutdown and reviews the MUT's demagnetization limit. Section III-C reviews the MUT's dynamics during an ASC. Section III-D treats the demagnetization objective, whereas Section III-E elaborates on the torque objective. Section III-F treats the impacts of speed variations. Finally, Section III-G discusses how the results can be used in an actual drive.

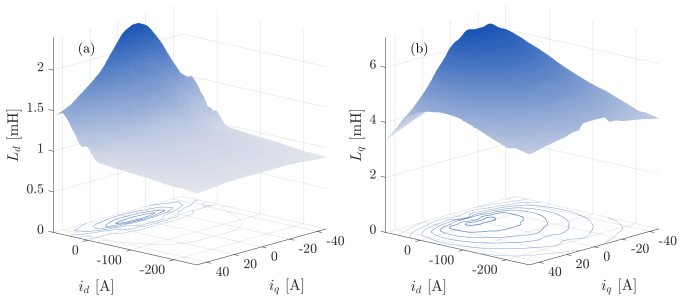

Fig. 1: Extrapolated and smoothened apparent inductance maps: (a) $L_d(\bar{i}_{dq})$ and (b) $L_q(\bar{i}_{dq})$.

TABLE I: Parameters of the BRUSA HSM1-6.17.12.

Phases	m_s	3	[-]
Pole pairs	p	3	[-]
Nominal power	P_N	70	[kW]
Nominal/Peak speed	$\omega_{m,N}$ / $\omega_{m,\text{pk}}$	3′600 / 12′000	[rpm]
Nominal/Peak torque	τ_N / τ_pk	130 / 320	[Nm]
Nominal current	I_N	202	[A_{pk}]
DC-link voltage	V_{dc}	400	[V]
Stator resistance	$R_s(60\,^\circ\text{C})$	48	[mΩ]
Critical UCG speed	$\omega_{m,\text{UCG}}$	5′600	[rpm]

A. Machine Under Test

The MUT in this study is the 70 kW commercial three-phase interior PMSM BRUSA HSM1-6.17.12 [11] shown in Fig. 2, and whose nameplate parameters are declared in Table I. It is used as a working example from this section onwards. Its apparent inductances, Fig. 1, are derived from experimentally identified flux maps and have been smoothened and extrapolated as described in Section II-D. The incremental inductances are found from the partial derivatives of these maps using finite differences.

B. Uncontrolled Generation and Demagnetization Limits

Inverter shutdown is the state when all inverter switches are turned off. This state is preferable to an ASC as long as the induced back-emf is lower than the reflected DC-link-voltage, $2V_{dc}/\pi$. Exceeding this voltage causes the anti-parallel diodes of the switches to turn on, resulting in UCG [6]. The critical speed, listed in Table I, for this condition is

$$\omega_{m,\text{UCG}} = \frac{2}{\pi}\frac{V_{dc}}{p\psi_{PM}}. \tag{9}$$



Fig. 2: The BRUSA HSM1-6.17.12 machine under test.

As seen, $\omega_{m,\text{UCG}}$ exceeds the nominal speed of the MUT and roughly corresponds to the speed at its maximum continuous power [11]. Although not quantified, this feature has been highlighted in the datasheet [11]. It means that the inverter can be shut down from all feasible speeds at both maximum and rated continuous torque without entering UCG. Therefore, inverter shutdown will in practice be preferred over an ASC for this machine, unless operated in field-weakening.

The machine's PMs demagnetize, at least partially, if the current trajectory during an ASC transient passes the demagnetization limit. This boundary is determined by the type of PMs mounted in the machine's rotor and their temperature [10, Ch. 3.7.4]. A positive d-current may also demagnetize the PMs but, in principle, this current is much larger than the negative demagnetization current. Therefore, it can normally safely be ignored.

The MUT's demagnetization limit is not declared in the datasheet and has not been experimentally characterized. Under the assumption that the machine has been designed such that its PMs do not demagnetize when short-circuiting the terminals at nominal speed and maximum torque when operated at MTPA, a coarse lower limit can be calculated by simulating the motor dynamics using (4) and retrieve the minimum d-current during the transient. Doing so results in the estimation $|i_{d,\text{demag}}| > 651\,\text{A}$. The experimental flux maps of the MUT have been identified in the ranges $-240\,\text{A} < i_d < 80\,\text{A}$ and $-45\,\text{A} < i_q < 45\,\text{A}$. Therefore, it is necessary to extrapolate the maps to calculate both the MTPA and the ASC trajectory starting from maximum torque and rated speed.

In summary, the machine appears to have been designed to withstand much higher demagnetization currents than the installed inverter limits (see Table I). To provide a working example, we therefore set a fictive demagnetization limit of $i_{d,\text{demag}} = |-250|\text{A}$. Furthermore, we will evaluate a relatively low speed of 500 rpm. This corresponds to $R_s^2/(L_d L_q \omega_r^2) = 1.017$ at the SSC, which is at the border where the SSC is little affected by the speed. The chosen speed and fictive demagnetization limit will together confine us within the experimentally determined flux-map region with only minor excursions into extrapolated areas. Altogether, we emphasize that the proposed methodology for calculating the ASC demagnetization safe operating area (SOA) of the MUT in this paper only should be considered a proof-of-concept.

C. Phase Portrait of the ASC Transient

Once the ASC is initiated, there is no degree of freedom left for the drive to control the dynamics of the system (4). I.e., the back-emf is the only driving force when $\bar{u}_{dq} = 0$. Consequently, the trajectory of the current vector can solely be influenced by controlling its initial value, $\bar{i}_{dq}(0)$. We shall now define what an acceptable ASC transient is and investigate how to determine initial values that result in such transients.

The flux maps of the considered PMSM together with the stator resistance completely characterize the electromechanical energy conversion of the machine. Hence, the ASC phase portrait in Fig. 3 is drawn by applying (4) at $\bar{u}_{dq} = 0$. It

depicts the time-derivative vector field of $\bar{i}_{dq}$ at a fixed speed, $500\,\mathrm{rpm}$, and temperature, $60\,^{\circ}\mathrm{C}$, without solution curves. For illustrative purposes, the vectors have been complemented by four colormaps, according to the following scheme:

- Yellow: $^{di_d}/_{dt} \geq 0$ and $^{di_q}/_{dt} \geq 0$.
- Orange: $^{di_d}/_{dt} \geq 0$ and $^{di_q}/_{dt} < 0$.
- Violet: $^{di_d}/_{dt} < 0$ and $^{di_q}/_{dt} \geq 0$.
- Blue: $^{di_d}/_{dt} < 0$ and $^{di_q}/_{dt} < 0$.

When plots of the demagnetization limits, $i_{d,\mathrm{demag}}$, and machine/inverter current limit, I_{max}, are superimposed along with the SSC at a specific speed, the phase portrait constitutes a constrained domain of currents and their dynamics. The MTPA trajectory of the PMSM is also added to illustrate the typical operating points under field-oriented control (FOC). By following it from the origin, it can be verified that the current derivative vectors increase in magnitude and rotate slightly in the counter-clockwise direction. This causes the current to take a wider spiraling trajectory towards the SSC, resulting in a larger transient current as illustrated by the dotted brick-colored infeasible example trajectory. Consequently, the transient demagnetization current increases with loading. This is consistent with the findings of [3], obtained using Monte Carlo simulations of 2500 randomly generated machine designs, and later confirmed analytically in [5].

D. Demagnetization Limit SOA

To not exceed the demagnetization boundary, it is required that $^{di_d}/_{dt}(|i_{d,\mathrm{demag}}|, i_q) \geq 0$ if the trajectory touches the demagnetization boundary at any time instance. Therefore, we search for the points $^{di_d}/_{dt}(|i_{d,\mathrm{demag}}|, i_q) = 0$ along the line $i_d = i_{d,\mathrm{demag}}$ in the phase-portrait to determine the safe and un-safe regions of the phase-plane.

A visual inspection of Fig. 3 suggests that $\mathrm{sgn}\left(^{di_d(I_d,i_q)}/_{dt}\right)$ changes solely at one point along the lines (I_d, i_q) for constant $i_d = I_d$. I.e. the blue and purple areas interface either the orange or yellow areas only once. This is not a requirement but is in principle an effect of the stable spiral that the lossy system dynamics in (4) constitute where the currents spiral monotonically to the SSC [5].

Next, the solutions $(i_{d,\mathrm{demag}}, i_{q,\mathrm{demag}})$ are set as initial values of an ordinary differential equation (ODE) solver to step backward in time. The inductance maps are interpolated to supply a more accurate derivative to the ODE solver. The resulting innermost trajectories denote new boundaries that, together with the demagnetization and inverter/machine current limit, define a SOA, drawn in green in Fig. 3. The boundary and interior of the SOA constitute feasible initial points during the operation of the drive and guarantee that $i_d(t) > -i_{d,\mathrm{demag}},\ t > 0$ once the ASC is initiated, provided the system spirals monotonically to the SSC.

It is assumed that the current can exceed the inverter/machine current limit during the ASC transient. Typically, this course is fast and will settle to the SSC within some hundreds of milliseconds, with a temporary overcurrent only lasting a fraction of that time. Indeed, Choi and Jahns show that the time constant of the magnetizing current during an ASC is $\tau_{\mathrm{ASC}} = {}^{2L_d}/_{(R_s(1+\xi))}$ for an unsaturated machine [3]. For the MTPA currents at rated speed and torque of the MUT, its per-unit parameter values are $R_s = 0.042$ and $L_d = 0.9$ with a saliency of $\xi = {}^{L_q}/_{L_d} = 5$. The time-constant is $\tau_{\mathrm{ASC}} = 7$, corresponding to $6.3\,\mathrm{ms}$ at $f_s = 180\,\mathrm{Hz}$. It is within the lower range of time constants evaluated in [3].

E. Torque Limit SOA

The procedure to delimit the SOA for the torque follows the same line of thought as delimiting the SOA for the demagnetization current but involves more calculations. We recall that the SOA is the set of initial conditions $\bar{i}_{dq}(0)$ that results in a current trajectory obeying $|\tau_e(t)| \leq \tau_{e,\mathrm{max}},\ t > 0$ at a fixed speed and temperature.

Fig. 4 plots the iso-torque lines of the MUT. Each quadrant of the $\bar{i}_{dq}$ state-space contains a delimiting iso-torque curve, $\pm\tau_{e,\mathrm{max}}$, which must not be exceeded during the ASC transient. The requirement for all $\bar{i}_{dq}$ resulting in $|\tau_e(\bar{i}_{dq})| = \tau_{\mathrm{max}}$ is formally equivalent to:

$$\begin{cases} \nabla\tau_e(\bar{i}_{dq}) \cdot \frac{d\bar{i}_{dq}}{dt} \geq 0, & \text{if } \tau_e < 0 \\ -\nabla\tau_e(\bar{i}_{dq}) \cdot \frac{d\bar{i}_{dq}}{dt} \geq 0, & \text{if } \tau_e > 0 \end{cases}. \tag{10}$$

Eq. (10) constitutes a gradient condition illustrated in Fig. 5. $\nabla\tau_e$ is always perpendicular to the iso-torque line, meaning that it will not be infringed at the next time-step, provided the current derivative-vector points inwards from the curve. Eq. (10) expresses this constraint by requiring that the angle φ between $\pm\nabla\tau_e(\bar{i}_{dq})$ and $^{d\bar{i}_{dq}}/_{dt}$ is in the interval $[-\pi/2,\ \pi/2]$.

We can now formulate a procedure for finding the torque SOA. Fig. 4 is provided as a reference with $\tau_{e,\mathrm{max}} = 100\,\mathrm{Nm}$, corresponding to $28\,\%$ of the MUT's peak torque.

1) Find the set of $\bar{i}_{dq}$ along one of the iso-torque curves $\pm\tau_{e,\mathrm{max}}$ that obeys (10), corresponding to the blue solid markers in Fig. 4. If no such points exist, $\tau_{e,\mathrm{max}}$ should be increased.
2) Step forward and backward from the first and last point obeying (10) (circled in sky blue) until a torque or demagnetization limit is intersected.
3) The generated trajectories, the current-limit circle and demagnetization limits constitute new boundaries.
4) Simulate from the next iso-torque line until all four have been evaluated. The innermost, most restrictive, among all boundaries is retained and updated between the simulations so that an enclosing boundary always exists.

The intersection of the calculated torque and demagnetization limits constitutes the ultimate SOA shaded in dark blue.

It is seen that the demagnetization limits enclose the safe torque region entirely. Consequently, the torque constraint is the limiting factor for the SOA in this example. A relaxed torque constraint or a higher speed (see Section III-F), however, would eventually infer that the demagnetization limit determines at least segments of the SOA boundaries.

F. Effects of Speed Variations

The speed impacts the SOA by altering its boundaries. Higher speeds correspond to a stronger driving force (back-

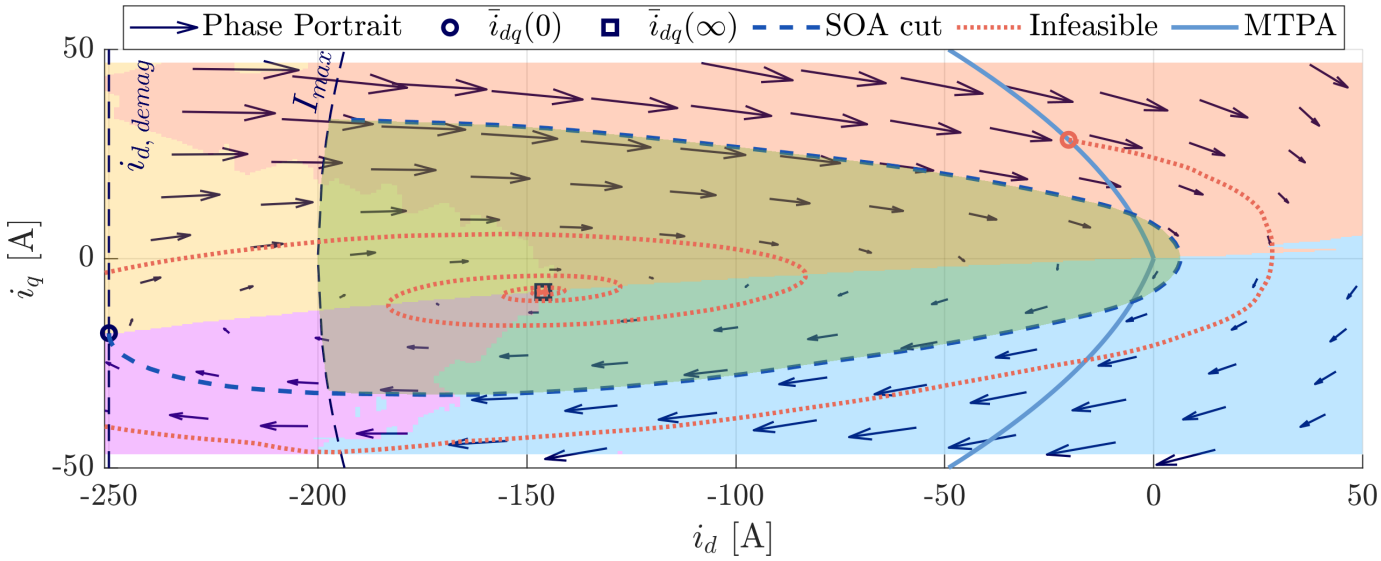

Fig. 3: Phase-portrait at $\omega_m = 500\,\mathrm{rpm}$ with the SOA (green) honoring the demagnetization and machine/inverter current limit.

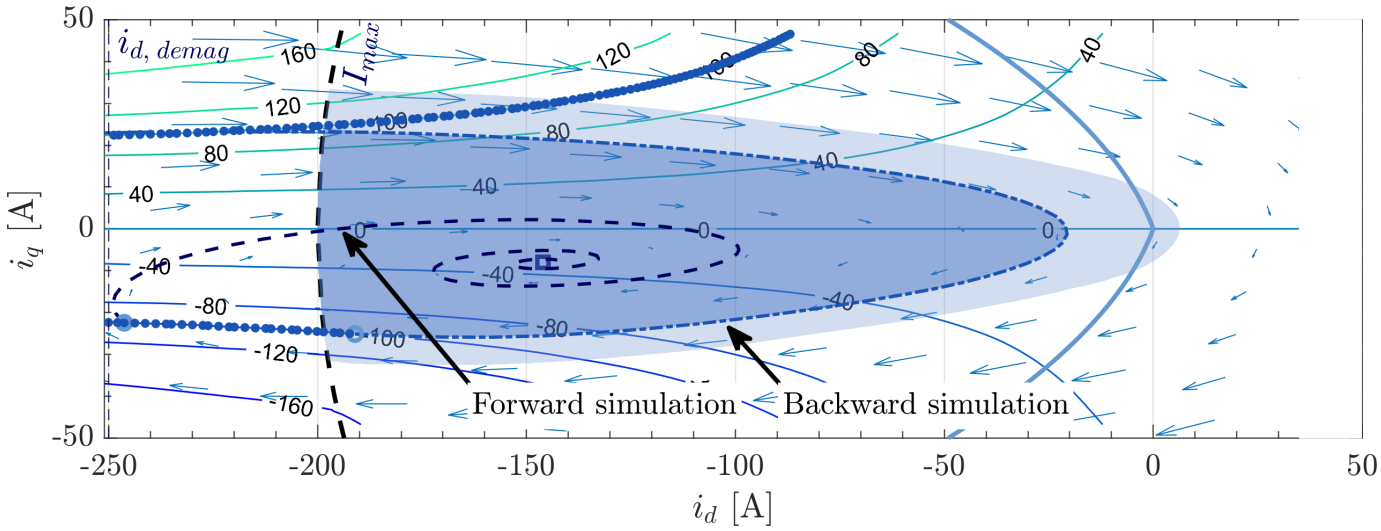

Fig. 4: Phase portrait at $\omega_m = 500\,\mathrm{rpm}$ with the SOA of the demagnetization limits (light shade) and the torque (dark shade). A square marks the SSC and the MTPA-trajectory is solid in sky blue. The iso-torque lines are labeled with τ_e in Nm.

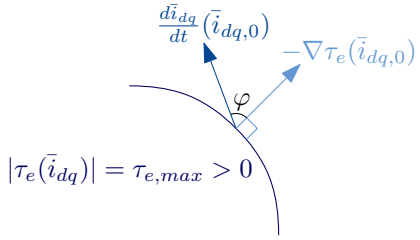

Fig. 5: Illustration of the gradient condition, (10), for the torque constraint.

emf), causing the SOA to shrink, as shown in Fig. 6 for (a) demagnetization and (b) torque boundaries. The demagnetization plot indicates a rapid reduction in the SOA from $\omega_m = 500\,\mathrm{rpm}$ to $\omega_m = 1000\,\mathrm{rpm}$, with a smaller decrease from $\omega_m = 1000\,\mathrm{rpm}$ to $\omega_m = 2250\,\mathrm{rpm}$, attributed to the resistive voltage drop's greater impact at low speeds. In contrast, the torque plot shows a mild influence of speed on the torque SOA. As the ASC primarily is used at high speeds where UCG is prohibitive, the combined SOA remains relatively constant for applicable speeds. Considering a broader speed range, however, the demagnetization limit has a more pronounced effect on SOA boundaries compared to the torque boundaries as speed increases.

In practical scenarios, speed variations are expected during the ASC transient. The vehicle's inertia greatly impacts these fluctuations and in a heavy vehicle, they are likely to be small. While the vehicle decelerates, SOA boundaries remain conservative estimates. Initially, a speed decrease is probable, but not guaranteed once the ASC begins. This is illustrated in Fig. 7 which plots the torque's time-derivative in state space during an ASC of the MUT. Orange areas signify decreasing torque, whereas blue areas indicate increasing torque. For

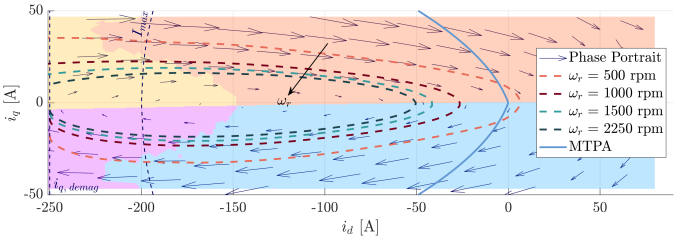

(a) Demagnetization limits.

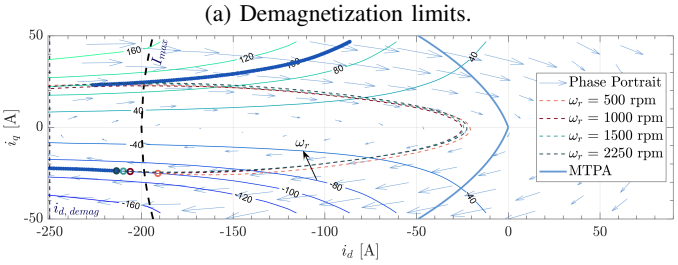

(b) Torque limits. Circles indicate the largest i_d for which (10) holds at each considered speed.

Fig. 6: SOA boundaries for different speeds. The phase portraits are drawn for $\omega_m = 2250\,\mathrm{rpm}$.

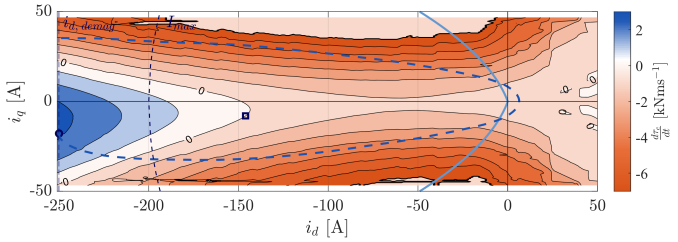

Fig. 7: Time derivative of the torque in state-space with demagnetization SOA (blue dashed), MTPA trajectory (sky solid), and SSC (navy square) at $\omega_m = 500\,\mathrm{rpm}$.

most initial operating points within the SOA and all points on the MTPA trajectory, the torque decreases at the start of the transient. As a result, a forward-moving vehicle then loses thrust, enters braking, or applies more braking torque during the first part of the ASC, leading to a likely speed decrease unless on a sufficiently steep downhill. Conversely, torque initially increases if the ASC starts in blue areas. Avoiding such situations is possible by excluding areas with positive torque derivatives from the SOA; a consideration mentioned in this paper without integrating such constraints.

G. Pre-ASC Control Strategy

The ISO26262 standard defines the fault tolerant time interval (FTTI) as the total elapsed time between a fault's occurrence and the initiation of a hazardous event due to the same fault [1]. Consequently, the system must detect it and enter a fail-safe state, possibly transitioning through an emergency operation, within the FTTI [1]. Modern current controllers are typically designed for rise times in the order of milliseconds [12]. In fact, a common recommendation to ensure the robustness of a model-based FOC using space-vector modulation is to select the rise time larger than $5\ln 9/(2\pi F_s)$ for a sampling frequency of F_s [12]. This translates into a switching frequency of at least $1.75\,\mathrm{kHz}$ for a desired rise-time of $1\,\mathrm{ms}$; a rather undemanding figure for state-of-the-art drives using silicon IGBTs or MOSFETs [12], [13]. These numbers indicate that the regulator can be designed to bring the current vector to a desired reference within a few milliseconds before entering the safe state. Thus, the initial state of the uncontrolled ASC, $\bar{i}_{dq}(0)$, should be selected within the computed SOA.

IV. Simulated Validation Using SyR-e

The open-source Synchronous Reluctance-Evolution (SyR-e) platform provides a combined machine design and simulation environment based on FEMM® and MATLAB®. It is freely available from [14]. SyR-e uses flux maps and their inverses to simulate dynamic machine models. Its accuracy has been validated multiple times against FEA simulations and experiments. Particularly, [5] thoroughly validates the accuracy of the flux-map-based model of the BRUSA motor in SyR-e subjected to an ASC versus experiments. Therefore, SyR-e is used in this paper to verify the current and torque trajectories of the non-linear inductance-based model of the MUT, (4), which determines the SOA.

Fig. 8 compares the time-domain current and torque of the model (4) with the subscript *traj* to those produced by SyR-e with the subscript *SyR-e*. The imposed speed is fixed to $500\,\mathrm{rpm}$ and the initial current vector is $\bar{i}_{dq}^{T}(0) = \vec{0}$ A.

Fig. 8a demonstrates that the current waveforms are practically identical throughout the entire transient and at steady state. Notice that the minimum d-current for which the flux-maps were identified is -240 A. Consequently, the flux maps, the apparent inductances, and the incremental inductances were extrapolated linearly and independently of one another beyond this value. The plot in Fig. 8b similarly compares the electromagnetic torque to that computed in SyR-e. Once again, the results are practically indistinguishable. We remark that the torque calculation in both SyR-e and the inductance-based model both implement (5) and, therefore, do not include possible torque ripple.

Fig. 9 displays another time-domain comparison between SyR-e and the inductance-based dynamic model. Now, the initial condition is $\bar{i}_{dq}^{T}(0) = [-198.0,\ \ 23.1]$ A which is at the intersection between the current-limit circle and the torque SOA in Fig. 4. Importantly, and as intended, the torque and current do not violate the limits imposed by the SOA, indicating that the proposed method accurately generates the torque, current, and demagnetization bounded ASC SOA.

Provided the stellar accuracy of the SyR-e model of the BRUSA motor demonstrated in [5], the conducted simulations give confidence in the accuracy of the SOA calculations using the proposed non-linear inductance-based transient model.

V. Conclusion

This paper introduces a rapid and interpretable mathematical/graphical approach for determining the SOA of initial

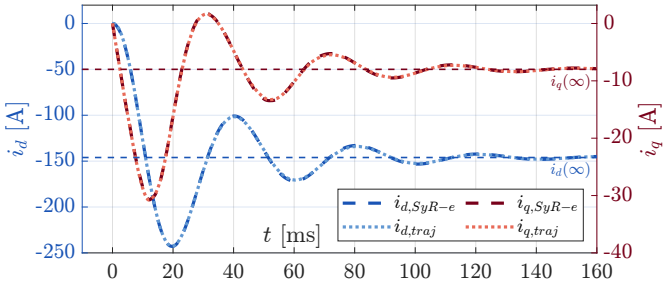

(a) Current.

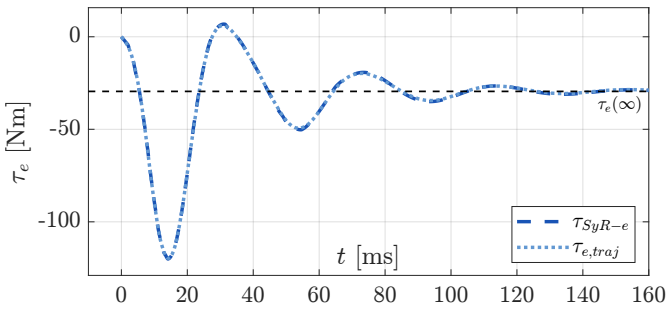

(b) Torque.

Fig. 8: Time-domain waveforms for the predicted trajectories compared to the output from SyR-e for $\bar{i}_{dq}^T = [0,\ 0]$ A.

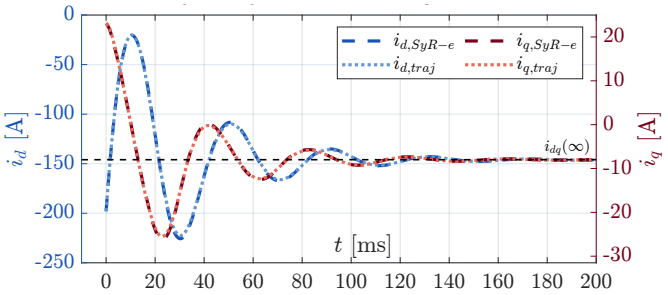

(a) Current.

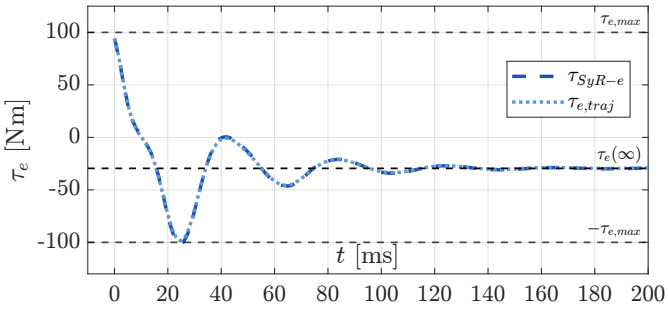

(b) Torque.

Fig. 9: Time-domain waveforms for the predicted trajectories compared to the output from SyR-e for the torque edge case $\bar{i}_{dq}^T(0) = [-198.0,\ 23.1]$ A.

conditions before applying an ASC to three-phase PMSMs. The SOA is defined by the set of initial $\bar{i}_{dq}$ leading to ASC transients respecting demagnetization current limits and a user-defined maximum torque. Commanding the current vector into the SOA prior to applying the ASC prevents PM demagnetization, and ensures passenger safety. The method relies on a dynamic non-linear model based on flux maps, identifiable experimentally or through FEA. A few offline dynamical simulations suffice to determine the entire SOA at a fixed speed, minimizing computational load. Our method improves on [5] by computing the complete map of safe initial conditions with less conservative boundaries. Speed variations' impact on the SOA is discussed using presented graphical methods. Validation in the open-source simulation platform SyR-e for a 70 kW commercial PMSM with experimentally identified flux maps affirms accuracy. The method is expected to be particularly useful in the development, initial testing, and commissioning of PMSMs in automobiles where functional safety standards must be fulfilled. Future research aims to experimentally validate the method on a real drive line.

References

[1] ISO/TC 22/SC 32, "ISO26262-1:2018," in *ISO26262-1:2018*, 2nd ed. International Organization for Standardization, 2018. [Online]. Available: https://www.iso.org/standard/68383.html

[2] S. Chen, X. Hao, C. Gao, and Z. Jiang, "An effective nontransient active short-circuit method for PMSM in electric vehicles," *IEEE Transactions on Industrial Electronics*, vol. 70, no. 4, pp. 3571–3580, 2023.

[3] G. Choi and T. M. Jahns, "Investigation of key factors influencing the response of permanent magnet synchronous machines to three-phase symmetrical short-circuit faults," *IEEE Transactions on Energy Conversion*, vol. 31, no. 4, pp. 1488–1497, 2016.

[4] B. Welchko, T. Jahns, W. Soong, and J. Nagashima, "IPM synchronous machine drive response to symmetrical and asymmetrical short circuit faults," *IEEE Transactions on Energy Conversion*, vol. 18, no. 2, pp. 291–298, 2003.

[5] S. Ferrari, G. Dilevrano, P. Ragazzo, P. Pescetto, and G. Pellegrino, "Fast determination of transient short-circuit current of PM synchronous machines via magnetostatic flux maps," *IEEE Transactions on Industry Applications*, vol. 59, no. 4, pp. 4000–4009, 2023.

[6] T. Jahns and V. Caliskan, "Uncontrolled generator operation of interior PM synchronous machines following high-speed inverter shutdown," *IEEE Transactions on Industry Applications*, vol. 35, no. 6, pp. 1347–1357, 1999.

[7] S. Ruoho, J. Kolehmainen, J. Ikaheimo, and A. Arkkio, "Interdependence of demagnetization, loading, and temperature rise in a permanent-magnet synchronous motor," *IEEE Transactions on Magnetics*, vol. 46, no. 3, pp. 949–953, 2010.

[8] S. Ferrari, P. Ragazzo, G. Dilevrano, and G. Pellegrino, "Flux and loss map based evaluation of the efficiency map of synchronous machines," *IEEE Transactions on Industry Applications*, vol. 59, no. 2, pp. 1500–1509, 2023.

[9] E. Armando, R. I. Bojoi, P. Guglielmi, G. Pellegrino, and M. Pastorelli, "Experimental identification of the magnetic model of synchronous machines," *IEEE Transactions on Industry Applications*, vol. 49, no. 5, pp. 2116–2125, 2013.

[10] J. Pyrhonen, T. Jokinen, and V. Hrabovcová, *Design of Rotating Electrical Machines*. John Wiley & Sons, Ltd, 2013, ch. 7, pp. 331–494.

[11] BRUSA Elektronik AG. HSM1-6.17.12 – BRUSA. Accessed: 2023-11-24. [Online]. Available: https://www.brusa.biz/portfolio/hsm1-6-17-12-2/

[12] L. Harnefors and H.-P. Nee, "Model-based current control of AC machines using the internal model control method," *IEEE Transactions on Industry Applications*, vol. 34, no. 1, pp. 133–141, 1998.

[13] S. Yang, Q. Wang, Z. Xie, X. Zhang, and L. Chang, "Digital current controller with a novel active damping design for IPMSM," *IEEE Transactions on Energy Conversion*, vol. 37, no. 1, pp. 185–197, 2022.

[14] F. Cupertino and G. Pellegrino, "SyR-e: Synchronous reluctance (machines) - evolution," https://github.com/SyR-e, Accessed: 2023-11-24.